Chinese Chemical Letters 37 (2026) 112246

Contents lists available at ScienceDirect

Chinese Chemical Letters

journal homepage: www.elsevier.com/locate/cclet

Non-thermal plasma synergistic regeneration for Pt catalyst performance reconstruction

Yunxi Shi[a], Dongjie Cheng[a], Yi Liu[a], Xinyi Huang[a], Pan Wang[a], Zhenguo Li[b], Jizhou Jiang[c,*]

[a] School of Automotive and Transportation Engineering, Jiangsu University, Zhenjiang 212013, China
[b] National Engineering Laboratory for Mobile Source Emission Control Technology, China Automotive Technology and Research Center Co., Ltd., Tianjin 300300, China
[c] School of Materials Science and Engineering, State Key Laboratory of Green and Efficient Development of Phosphorus Resources, Engineering Research Center of Phosphorus Resources Development and Utilization of Ministry of Education, Key Laboratory of Green Chemical Engineering Process of Ministry of Education, Hubei Key Laboratory of Plasma Chemistry and Advanced Materials, Novel Catalytic Materials of Hubei Engineering Research Center, Wuhan Institute of Technology, Wuhan 430205, China

ARTICLE INFO

Article history:
Received 20 August 2025
Revised 4 December 2025
Accepted 9 December 2025
Available online 10 December 2025

Keywords:
Diesel oxidation catalysts
Sintering of Pt
Non-thermal plasma
Regeneration

ABSTRACT

Aging of Pt in diesel oxidation catalyst (DOC) leads to diminished catalytic activity, presenting a considerable challenge for catalyst regeneration and enhancement. This work investigates on the regeneration of Pt/Al_2O_3-SiO_2 (Pt/AS) catalysts in DOC utilizing the synergistic effect of the indirect non-thermal plasma (INTP) and direct non-thermal plasma (DNTP) to optimize catalytic performance for efficient and stable conversion of gaseous pollutants. The distinctive properties of DNTP-INTP promote the removal of surface particulate matter (PM) and increase the availability of adsorbed oxygen (O_{ads}) on the catalyst surface. Moreover, DNTP effectively reduces the particle size of sintered catalysts by applying a high-energy electric field. This process facilitates the conversion of PtO_x to metallic Pt^0. Additionally, agglomerated Pt structures can be reverted into regular hexahedral nanoparticles through the synergistic process. The regenerated catalyst demonstrates exceptional catalytic performance and stability, which can rival the performance of newly prepared catalysts. Notably, compared to the aged catalyst, the low-temperature performance improves significantly, with a reduction of 90 °C in the temperature at the onset of catalytic activity. These results highlight the considerable potential of plasma-assisted synergistic catalysts regeneration for revitalizing aged DOC within the context of advancing clean energy technologies.

© 2026 Published by Elsevier B.V. on behalf of Chinese Chemical Society and Institute of Materia Medica, Chinese Academy of Medical Sciences.

The environment serves as the cornerstone of sustainable development. The Euro VII emission regulations, implemented on April 12, 2024, exemplify the ongoing enhancements in emission standards and environmental policies. These advancements have significantly contributed to the consistent mitigation of detrimental pollutants discharged by fuel-powered vehicles. While diesel engines typically exhibit superior fuel efficiency compared to gasoline engines, issues such as incomplete combustion lead to the emission of harmful pollutants (CO, NO, hydrocarbons, and PM), which pose serious health risks to humans [1–5]. Currently, the primary method for addressing CO and other contaminants involves the incorporation of a diesel oxidation catalyst (DOC) into the aftertreatment system [6–9]. The DOC utilizes catalysts derived from platinum group metals (PGMs) that are coated within the channels to facilitate the conversion of exhaust pollutants into CO_2 and NO_2. The presence of PM and harmful gases in the exhaust stream leads to carbon accumulation and contamination on the surface of the DOC. Furthermore, the extreme conditions of elevated temperature and pressure in the exhaust gas contribute to the degradation of the noble metal catalyst coating through a process known as sintering. Collectively, these adverse factors result in the deactivation of the DOC and a subsequent reduction in its catalytic efficiency [10–13]. Currently, common methods for rejuvenating aged DOC include thermal regeneration and wet washing regeneration. However, traditional thermal regeneration is energy-intensive and promotes catalyst agglomeration and sintering, which leads to a reduction in catalytic efficiency. Chemical approaches like wet washing are ineffective in removing surface-covered PM and can cause secondary pollution due to the excessive use of chemical reagents. Therefore, there is an urgent need for novel regeneration techniques for aging DOC [14–17].

* Corresponding author.
E-mail address: 027wit@163.com (J. Jiang).

https://doi.org/10.1016/j.cclet.2025.112246
1001-8417/© 2026 Published by Elsevier B.V. on behalf of Chinese Chemical Society and Institute of Materia Medica, Chinese Academy of Medical Sciences.

Non-thermal plasma (NTP) represents a promising technology for regeneration [18–24]. In particular, dielectric barrier discharge (DBD) plasma, a prevalent form of NTP, is widely employed in catalyst preparation and modification. NTP are classified into indirect NTP (INTP) and direct NTP (DNTP) based on their distinct operational mechanisms. INTP functions by generating high-energy electrons through electrical discharge rather than by heating the gas. This process creates various environments (ions, radicals, electrons, photons, and excited molecules) that facilitate oxidation, reduction, or non-reactive reactions. The resulting chemically active species then interact with the surface of nanomaterials, inducing changes in their physical and chemical properties. This optimization of electronic structure imparts the desired properties to the nanomaterial [25,26]. Zhu *et al*. utilized NTP for the purification of volatile organic compounds (VOCs) and integrated it with a selective catalytic reduction (SCR) catalyst to enhance pollutant removal efficiency [27]. Kim *et al*. investigated the application of a packed bed reactor for plasma-generated monoatomic oxygen and ozone treatment of Au/TiO_2 to facilitate catalyst regeneration [28]. NTP with oxygen as the gas source generates abundant active species (O^*, O_3) for pollutant removal, thereby promoting the exposure of more active sites. Shi *et al*. demonstrated that NTP active species can efficiently eliminate diesel exhaust particulates at low temperatures through oxidation [29]. However, the indirect effect of NTP active species do not facilitate the reversible alteration of particle size and dispersion in sintered catalysts. It is widely acknowledged that reducing the size of metal nanoparticles can significantly enhance catalytic activity in various reactions by exposing more catalytically active corner or edge sites on the metal surface [30]. DNTP is commonly employed for the synthesis of highly dispersed metal nanoparticles at the nanoscale. In DOC, Pt catalysts tend to form PtO_x clusters under high-temperature and high-pressure conditions in exhaust gases. However, PtO_x ($x > 2$) exhibits limited catalytic activity towards the oxidation of gaseous pollutant [31]. Hwang *et al*. observed that at 600.0 °C, PtO_2 decomposes into Pt, which subsequently interacts with Al_2O_3 to form $PtAl_2O_4$ [32]. The electron temperature of DNTP discharge can reach up to 1.9726×10^4 °C or higher, while the bulk temperature typically remains below 200.0 °C [33]. The high-energy electrons generated by DNTP effectively reduce PtO_x in aged DOC. Zhang *et al*. synthesized a niobium carbide monoatomic catalyst using arc discharge with CH_4 as the gas source. This research successfully achieved the preparation of nano or even monoatomic single-atom catalysts (SAC) through the direct application of DNTP [34]. Borra *et al*. discovered that the interaction sites between DBD plasma filaments and various metal electrodes can induce localized vapor fluxes. This process results in the formation of primary metal nanoparticles through physical nucleation within expanding vapor jets, thereby producing diverse nanoparticles *via* DNTP [35]. Jiang *et al*. employed plasma techniques to fabricate a $LaMnO_3$ nano-network supported palladium catalyst, which enhances its surface area and porosity, demonstrating outstanding catalytic efficacy [36]. Yu and colleagues successfully mitigated coking by enhancing metal dispersion, decreasing the Ni particle size, and altering the Ni structure as a whole using a DNTP-assisted Ni-Pt catalyst [37]. The DNTP treatment facilitated reversible modifications in the morphology and dispersion of the sintered catalyst while notably enhancing the metal-support interaction. In a separate study, Liu *et al*. demonstrated that plasma treatment could strengthen the interaction between Ni and ZSM-5 support, effectively restraining the aggregation of noble metal catalysts [38]. Additionally, INTP technology enables the elimination of PM, nitrogen oxides, and carbon monoxide, thereby exposing the active sites of the catalyst. DNTP technology allows for the reversible alteration of the dispersion and morphology of sintered noble metal catalysts, thereby enhancing the interaction between the catalyst and the support material. However, limited research has been conducted on the impact of INTP and DNTP collaborative regeneration on the catalytic efficacy of aged DOC.

In this work, DNTP and INTP were utilized synergistically manner to rejuvenate aged DOC under ambient temperature and atmospheric pressure conditions (Figs. S1 and S2 in Supporting information). The objective was to explore the distinct regeneration outcomes resulting from various NTP regeneration approaches, while addressing the challenge of DOC deactivation. The ultimate goal was to restore the low-temperature reactivity and thermal stability characteristics of the aged catalyst, thereby achieving synergistic enhancement through the combined application of DNTP and INTP (Fig. 1). CO conversion and durability cycling experiments were conducted to assess the performance variations of DOC following deactivation and rejuvenation. Additionally, aged, fresh, and rejuvenated catalyst specimens were analyzed to investigate the effects of INTP and DNTP on the structure, morphology, elemental composition, and state of the aged catalyst. This investigation provides novel insights into the rejuvenation of aged catalysts and integrating plasma treatment technology into the catalytic filed, proposing a new research avenue for achieving enhanced catalytic efficacy and stability.

A clean DOC sample labeled as Fresh. In the initial phase of testing, apply an engine bench load of 75 % was applied while maintaining a constant rotation speed of 2500.0 r/min. The clean DOC was installed at the rear of the engine exhaust. After the diesel engine after treatment system had operated for 12.0 h, the aged DOC was designated as Pt/AS-1. Under atmospheric conditions, the catalyst was subjected to a discharge voltage of 10.0 kV for a duration time of 1.0 h. Direct electric shock aging using DNTP was applied to the DOC, resulting in a sample denoted as Pt/AS-2-D. In an O_2 atmosphere, an input voltage of 30.0 kV was applied for a discharge duration of 1.0 h to indirectly treat the aged DOC with INTP, yielding in the sample Pt/AS-3-I. Subsequently, INTP-DNTP synergistic regeneration treatment based on the previous step was performed to acquire the sample Pt/AS-4-I/D. Fig. S3 (Supporting information) shows the discharge parameters.

To investigate the impact of plasma regeneration on the catalytic oxidation performance of aging DOC, a series of CO catalytic oxidation performance tests were conducted. This study compared changes in characteristic temperatures, including T_S (the temperature at the onset of CO conversion), T_{50} (the temperature at 50 % CO conversion), and T_{90} (the temperature at 90 % CO conversion). Fig. 2a illustrates the temperature-dependent CO conversion efficiency of five groups of regenerated catalysts: Fresh, Pt/AS-1, Pt/AS-2-D, Pt/AS-3-I, and Pt/AS-4-I/D. As the noble metal catalyst reaches its light-off temperature, the conversion efficiency steadily increases with temperature until it reaches 100 %. Fig. 2b presents the characteristic temperatures (T_S, T_{50}, and T_{90}) for the different catalysts, which directly correlate with catalytic activity. A comparison with the fresh catalyst revealed that the TS of the aged Pt/AS-1 catalyst increased by 89.0 °C, primarily attributed to sintering and carbon deposition on the DOC surface due to prolonged operation, which led to decreased performance at lower temperatures. Following NTP treatment, the T_s values of Pt/AS-2-D, Pt/AS-3-I, and Pt/AS-4-I/D shifted towards lower temperatures, indicating an enhancement in catalytic performance at lower temperatures. Specifically, compared with Pt/AS-1, the regenerated catalysts Pt/AS-2-D, Pt/AS-3-I and Pt/AS-4-I/D exhibited reductions in T_S of 90.0, 93.0 and 93.0 °C. These findings suggest that NTP treatment effectively enhances the catalytic performance of aged catalysts at lower temperatures.

The data indicates that the T_{50}/T_{90} values of the Pt/AS-2-D and Pt/AS-3-I catalysts, treated solely with NTP, are significantly lower than those of the aged Pt/AS-1 catalyst sample. Notably, the Pt/AS-4-I/D sample, which underwent to INTP-DNTP synergistic regeneration treatment, exhibits the most pronounced decrease, with T_{50}

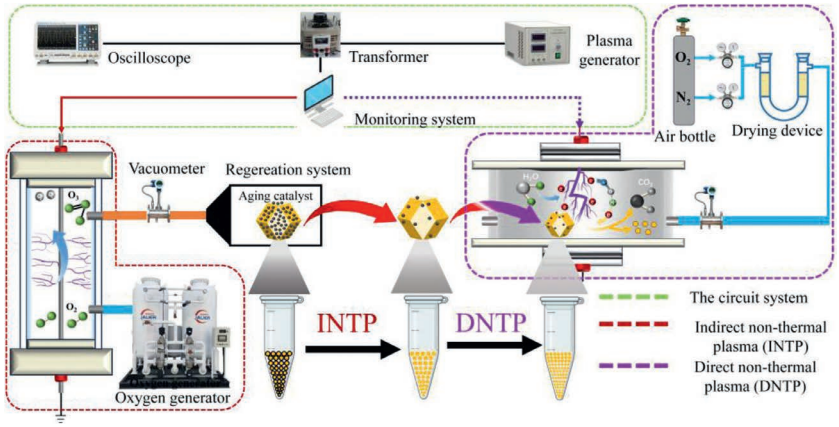


Fig. 1. Schematic diagram of the NTP regeneration system.

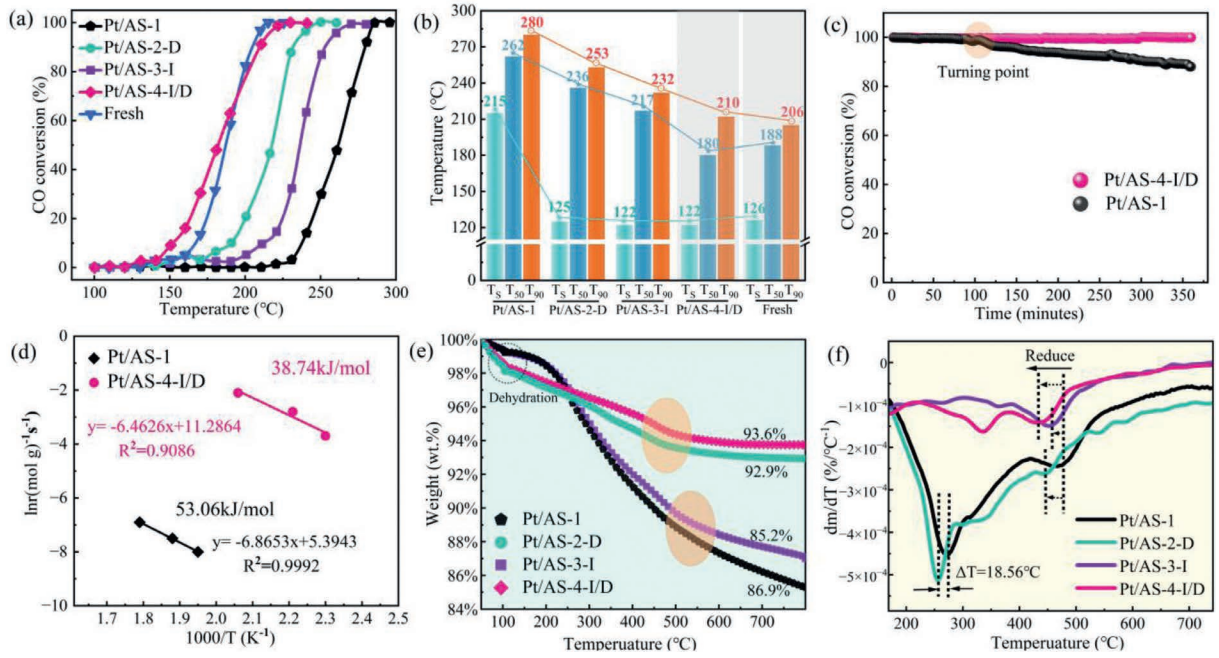


Fig. 2. (a) Plots of CO oxidation conversion rates for different catalyst samples. (b) CO oxidation performance of catalysts at different temperatures. (c) Stability test data curve of CO conversion catalyst. (d) Arrhenius plots of CO oxidation on different catalysts (Pt/AS-1, Pt/AS-4-I/D). (e) TG curves of regenerated and aged catalyst samples. (f) DTG curves of regenerated and aged catalyst samples.

decreasing by 82.0 °C and T_{90} by 70.0 °C. Remarkably, the T_{50} value of the Pt/AS-4-I/D sample (180.0 °C) is slightly lower than that of the fresh DOC sample (188.0 °C), while the T_{90} value (210.0 °C) is marginally higher than that of the fresh DOC sample (206.0 °C). Additionally, the temperature required for complete CO conversion is significantly reduced following NTP regeneration. These findings suggest that NTP regeneration treatment effectively enhances the catalytic oxidation performance of aged catalysts [39], with the most notable improvement observed in the aged DOC samples after INTP-DNTP synergistic regeneration treatment.

Fig. S4a (Supporting information) shows the catalytic oxidation data curves for toluene across all DOC samples. The conversion rate curves for the five catalyst groups exhibit similar trends: Once the precious metal catalysts reach their ignition temperature, conversion efficiency continuously increases with rising temperature until ultimately reaching 100%. Fresh DOC exhibits the highest catalytic activity, while the aged DOC sample Pt/AS-1 shows the lowest activity. After NTP treatment, the characteristic temperatures of Pt/AS-2-D, Pt/AS-3-I, and Pt/AS-4-I/D all shifted toward lower temperatures, significantly enhancing their catalytic activity. The catalytic activity of specific samples, ranked from highest to lowest, is: Fresh > Pt/AS-4-I/D > Pt/AS-3-I > Pt/AS-2-D > Pt/AS-1. Fig. S4b and Table S1 (Supporting information) lists the characteristic temperatures for toluene catalytic oxidation across catalyst samples. Compared to Pt/AS-1, Pt/AS-3-I and Pt/AS-4-I/D exhibited the greatest catalytic activity enhancement. The characteristic temperatures T_{max} for Pt/AS-3-I and Pt/AS-4-I/D increased by 18.7 °C and 18.0 °C, respectively. while Pt/AS-2-D exhibited an 8.7 °C increase in T_{max}. The catalytic oxidation capabilities of Pt/AS-3-I and Pt/AS-4-I/D were comparable. Catalytic oxidation results demonstrate that NTP regeneration can effectively restore the catalytic oxidation capacity of aged catalysts toward toluene. Unlike CO oxidation results, Pt/AS-4-I/D failed to fully recover the lost performance of Pt/AS-1.

The Arrhenius relation was utilized to calculate the activation energy of the catalyst (Fig. S5 in Supporting information). As shown in Fig. 2d, the activation energy of the Pt/AS-1 catalyst significantly decreased from 58.06 kJ/mol to 38.74 kJ/mol follow-

ing the INTP-DNTP synergistic regeneration treatment. Studies indicates a direct correlation between reduced activation energy and enhanced catalyst activity. Specifically, the order of catalytic activity is as follows: Pt/AS-1 (58.06 kJ/mol) > Pt/AS-2-D (46.71 kJ/mol) > Pt/AS-3-I (42.50 kJ/mol) > Pt/AS-4-I/D (38.74 kJ/mol), which corresponds with the CO conversion. These results collectively demonstrate the efficacy of the INTP-DNTP synergistic regeneration system in revitalizing and restoring the catalytic oxidation capabilities of aged catalysts.

Maintaining the effectiveness of DOC in removing of automotive emission pollutants such as CO, hydrocarbons, and NO_x at low temperatures, while ensuring stability under frequent high-temperature fluctuations, presents a critical challenge in emission reduction. To evaluate the durability of these catalysts under simulated automotive exhaust conditions at 250.0 °C, five groups of catalyst samples underwent cycling tests (Fig. S6 in Supporting information). The focus was on assessing the continuous oxidation conversion rate of CO. Notably, Pt/AS-4-I/D exhibited exceptional stability during endurance testing, as illustrated in Fig. 2c. In comparison to Pt/AS-1, Pt/AS-4-I/D maintained a consistently high and stable CO conversion rate. Conversely, Pt/AS-1 demonstrated a significant decline in CO conversion efficiency after 100.0 min of cycling, with efficiency progressively decreasing with extended cycle durations.

To further explore the thermal stability of the catalytic samples, thermal gravimetry (TG) was employed to assess the regenerated catalyst samples. The TG analysis reveals a weight reduction for Pt/AS-1, Pt/AS-2-D, Pt/AS-3-I, and Pt/AS-4-I/D of approximately 13.1 %, 14.8 %, 7.1 %, and 6.4 %, respectively, as the temperature increases from 25.0 °C to 800.0 °C (Fig. 2e). Specifically, Pt/AS-1 and Pt/AS-2-D exhibit a gradual decomposition trend beyond 500.0 °C, whereas Pt/AS-3-I and Pt/AS-4-I/D continue to degrade steadily after reaching 500.0 °C, indicating ongoing oxygen loss from the material's surface. The removal of oxygen from a material's surface can occur through three mechanisms: OH desorption [40], carbonate species decomposition [41], or direct desorption [42]. The differential thermogravimetry (DTG) results depicted in Fig. 2f reveal an exothermic peak around 250.0–260.0 °C, attributed to the ongoing condensation reaction of surface hydroxyl groups and the phase transition of the γ-Al_2O_3 carrier structure [43,44]. The subsequent weight loss stage between 450.0 °C and 480.0 °C primarily results from particles adhering to the DOC channels and the decomposition of noble metal oxides (PtO_x). The peak oxidation temperatures of Pt/AS-2-D, Pt/AS-3-I, and Pt/AS-4-I/D shift to lower temperatures compared to Pt/AS-1, suggesting enhanced low-temperature oxidation efficiency of the catalysts following plasma regeneration modification. The integration of endurance cycle assessments of catalyst samples and weight loss rate profiles further supports the initial inference of improved thermal stability of both the Pt catalyst and its support after NTP treatment.

In a DOC work environment, the accumulation of excessive coke on noble metal catalyst surfaces during fuel combustion can impede the interaction between active sites on the catalyst and reactive substances (CO, NO), thereby diminishing the catalytic oxidation efficiency towards pollutants in Fig. 3a. Therefore, the effective elimination of carbon deposits and other contaminants from the catalyst surface is of paramount importance for restoring and enhancing catalytic performance. Energy dispersive spectroscopy (EDS) elemental mapping images in Figs. 3b-g, which reveal notable differences [45]. Specifically, compared to the aged Pt/AS-1 catalyst, the Pt dispersion in the Pt/AS-2-D sample after DNTP treatment is markedly enhanced in Fig. 3h and Fig. S9 (Supporting information), as previously reported. Furthermore, the surface-bound carbon on the Pt/AS-3-I sample is effectively eliminated following INTP treatment (Fig. S8 in Supporting information). These findings align with prior research demonstrating the efficacy of NTP in removing carbon deposits from diesel exhaust emissions [46]. Fig. 3i and Fig. S7 (Supporting information) presents the elemental composition as determined by EDS surface scanning and XPS semi-quantitative analysis. The data in Table S2 reveals a notable decrease in the carbon content of the Pt/AS-3-I sample following INTP treatment, with the carbon content decreasing from 11.48 % in the Pt/AS-1 aged sample to 9.64 % in the Pt/AS-3-I sample. Fig. 3j illustrates that the trend in carbon content change observed in the XPS data aligns with the EDS results. Specifically, after INTP treatment, the carbon content in Pt/AS-1 samples decreased from 39.77 % to 24.01 % in Pt/AS-3-I samples. Fig. 3k shows a significant increase in Pt content in DOC due to carbon removal following plasma treatment. Subsequent after DNTP treatment resulted in a slight additional decrease in carbon content. Utilizing O_2 as the gas source in plasma generation leads to the production of abundant active species (O^*, O_3) that effectively eliminate PM at low temperatures [47], Fig. S10 (Supporting information) shows the oxygen element mapping results on the DOC surface, consistent with prior research [48,49]. The removal of carbon deposits is advantageous for restoring catalyst performance.

X-ray photoelectron spectroscopy (XPS) analysis was conducted to elucidate the valence state and electronic structure of the regenerated catalyst (Fig. 3l). Figs. 3m-n present the XPS spectra of Pt 4f and Al 2p The Pt 4f spectrum exhibits two peaks (Pt $4f_{7/2}$ and Pt $4f_{5/2}$) with lower binding energies at 70.69 and 73.89 eV, which correspond to Pt^0 species. Additionally, peaks at 71.67 and 75.17 eV are assigned to Pt^{2+} species, while peaks at 73.56 and 76.76 eV are designated as Pt^{4+} species. Analysis of Table S3 (Supporting information) indicates that the Pt^0 content across the five sample groups follows the order of Pt/AS-4-I/D > Fresh > Pt/AS-2-D > Pt/AS-3-I > Pt/AS-1. The Pt^{2+} content ranks as Fresh > Pt/AS-3-I > Pt/AS-2-D > Pt/AS-4-I/D > Pt/AS-1; and the sequence for Pt^{4+} content is Pt/AS-1 > Pt/AS-3-I > Pt/AS-2-D > Pt/AS-4-I/D > Fresh. Analysis of Pt 4f spectra indicates that Pt predominantly exists in the Pt^{4+} high oxidation state in aged catalyst samples, which is attributed to the oxidation of engine exhaust in high-temperature, oxygen-rich conditions. NTP treatment significantly alters the chemical valence state of Pt, with variations observed following different NTP treatments. The high oxidation state of Pt^{4+} in Pt/AS-1 was converted to metallic Pt^0 after DNTP treatment, while the high oxidation state of Pt^{4+} was converted to the metallic state Pt^{2+} after INTP treatment. The Pt^0 content in Pt/AS-4-I/D after INTP-DNTP synergistic regeneration treatment was the highest, and the increase of Pt^0 content suggests that there was a large amount of metallic Pt on the surface of the catalyst. Conversely, the aging catalyst Pt^{4+} was primarily converted to Pt^{2+} following the indirect regeneration by plasma active substances. The decrease in the valence state indicates that the precious metal oxides are effectively reduced. The excessive stability of Pt^{2+} contributes to its inactivity towards CO oxidation at low temperature, while the activity of Pt nanoparticles formed after reduction activation is enhanced [50,51]. This also explains why the oxidation ability of catalyst samples after NTP regeneration at low temperature is significantly higher than that of aging catalysts. The increased CO oxidation efficiency of Pt/AS-2-D and Pt/AS-4-I/D at low temperatures can be attributed to the direct impact of DNTP on aged catalysts, which facilities the formation of Pt single atoms. This process significantly enhances catalytic activity, complementing the intrinsic high catalytic efficacy of Pt species in the Pt^0 electronic state. Huizinga *et al*. observed a decrease in the binding energy of Pt supported on alumina as Pt particles sintered, attributing this phenomenon to the enhanced shielding of core holes by the electrons of neighboring atoms in larger particles. It is evident that the Pt peak position shifts towards higher binding energies for samples treated with equal DNTP regeneration. Notably, the peak position undergoes the most significant shift following INTP-DNTP

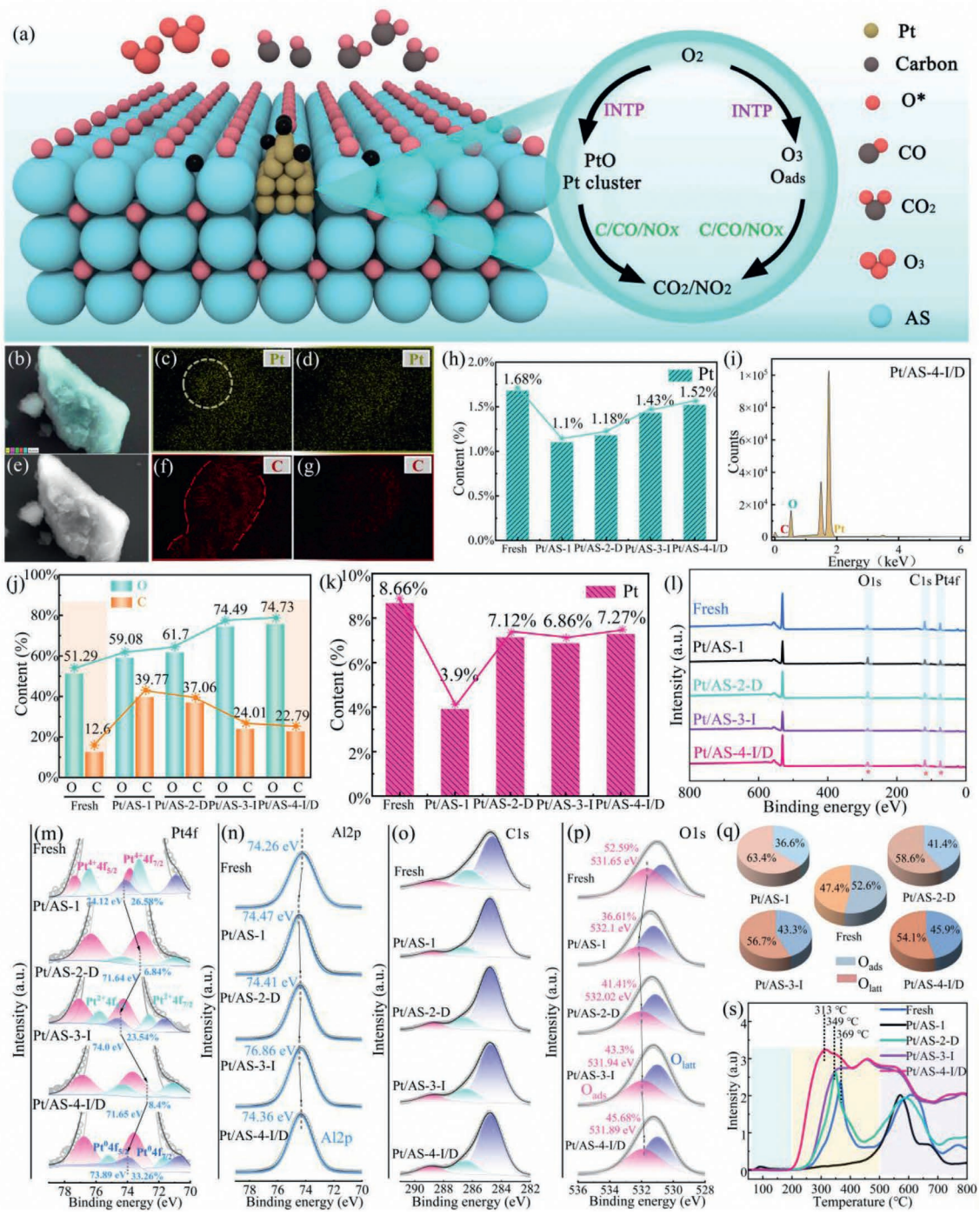


Fig. 3. (a) Schematic diagram of the mechanism of action of INTP. (b, e) SEM plots (Pt/AS-4-I/D). (c) The EDS surface scan image of Pt element on the Pt/AS-1 sample. (d) The EDS surface scan image of Pt element on the Pt/AS-2-D sample. (f) The EDS surface scan image of carbon on the Pt/AS-1 sample. (g) The EDS surface scan image of carbon on the Pt/AS-3-I sample. (h) Pt elemental content (XPS). (i) EDS energy spectrum. (j) C and O elemental content (XPS). (k) Pt elemental content (EDS). (l) XPS full spectrum. XPS fine spectra of Pt 4f (m), Al 2p (n), C 1s (o) and O 1s (p). (q) XPS catalyst adsorbed oxygen/lattice oxygen content. (s) O_2-TPD of five catalyst sample sets.

synergistic regeneration treatment, aligning well with the reported Pt^0 binding energy value. Analysis of the data presented in Table S5 (Supporting information) reveals varying degrees of a shift towards lower binding energies in the Al 2p peak position of the support following NTP regeneration. Compared to the Al 2p peak position in Pt/AS-1, the Al 2p peak position shifts to a lower binding energy, with shifts of approximately 0.08 eV and 0.13 eV for DNTP and INTP, respectively. Notably, the Pt 4f peak position of the catalyst shifts towards higher binding energies after NTP regeneration, with the most significant shift observed in DNTP regeneration. The Pt 4f peak position of Pt/AS-2-D shifts by 3.36 eV in comparison to the aged Pt/AS-1 catalyst. Fig. S11 (Supporting information) shows the Pt $4d_{5/2}$ spectral regions for five groups of Pt catalyst samples: aged DOC, fresh DOC, and NTP regenerated samples. After background subtraction from the scattered electron spectra using the Shirley method approximation and decomposing the spectra into individual components, two platinum states were identified in the catalysts: E_b(Pt $4d_{5/2}$) = 314.4–314.7 eV for the metallic state and an oxidized platinum state with E_b(Pt $4d_{5/2}$) = 317.6–318.2 eV. Table S8 (Supporting information) lists the metallic and oxidized

state contents in the catalyst samples. Table S6 (Supporting information) indicates the order of metallic Pt content among the five samples: Pt/AS-4-I/D > Fresh > Pt/AS-2-D > Pt/AS-3-I > Pt/AS-1. Although Pt 4f and Pt 4d yield different results for Pt valence state distribution, their trends align with the Pt 4f findings. Specifically, NTP coupling treatment of aged catalysts promotes the conversion of oxidized Pt in aged DOC to metallic Pt, significantly increasing the metallic Pt content even surpassing that in fresh DOC. Furthermore, the detailed analysis of the C 1s spectrum reveals energy levels of 289.1 eV for C=O, 286.5 eV for C–O, and 284.7 eV for C–C, as reported in a previous study in Fig. 3o [52].

Fig. 3p presents an analysis of O 1s spectra used to distinguish various oxygen species. The peak observed at a lower binding energy (530.8 eV) in the O 1s spectrum corresponds to lattice oxygen (O_{latt}), while the peak at a higher binding energy (531.7 eV) corresponds to adsorbed oxygen (O_{ads}) [53–55]. The proportion of O_{ads} is illustrated in Fig. 3q. Table S4 presents that the O_{ads} content in catalyst samples treated with different NTP increases to varying extents. Following regeneration, the O_{ads} content of the Pt/AS-4-I/D, Pt/AS-3-I, and Pt/AS-2-D samples increases by 4.8 %, 6.7 %, and 9.3 %, respectively, compared to the aged catalyst. The $O_{ads}/O_{ads}+O_{latt}$ ratio is ranked as follows: Fresh > Pt/AS-4-I/D > Pt/AS-3-I > Pt/AS-2-D > Pt/AS-1. Research indicates that a higher $O_{ads}/O_{ads}+O_{latt}$ ratio leads to increased generation of active oxygen and enhanced catalytic activity [56]. Notably, the $O_{ads}/O_{ads}+O_{latt}$ content of Pt/AS-4-I/D, modified by INTP-DNTP synergistic regeneration, significantly increases from 36.61 % to 45.86 % compared to Pt/AS-1. Furthermore, the $O_{ads}/O_{ads}+O_{latt}$ content of Pt/AS-4-I/D, modified by INTP-DNTP synergistic regeneration, approaches 52.59 % of that of the Fresh sample, indicating that INTP-DNTP can effectively enhance the O_{ads} content of Pt/AS-4-I/D. For Pt catalysts supported on inert materials, the primary reaction pathways involve the adsorption of mobile molecular oxygen on the support, its dissociation at the interface, and reactions at the interface between Pt particles and CO adsorbed on Pt. For Pt loaded on inert materials, reactive oxygen species (ROS) supply likely originates from either directly dissociated adsorbed O_{ads} on Pt particles or adsorbed O_{ads} on the support. The size of Pt particles plays a decisive role. Therefore, in INTP-DNTP systems, INTP generates active species that effectively remove particulate matter, while O_{ads} replenished on the Pt surface from aged DOC provide ROS for sustained catalytic CO oxidation of regenerated DOC.

To investigate the oxygen species involved in the reaction, the catalyst underwent oxygen temperature programming desorption (O_2-TPD) characterization. Fig. 3s presents the results, revealing distinct oxygen desorption peaks for both aged and regenerated catalyst samples. The O_2-TPD curve is delineated into three segments: Surface-adsorbed oxygen species ($O_2^-{}_{ad}$, 50–200.0 °C), chemisorbed oxygen species (O^-_{ad}, 200–500.0 °C), and bulk lattice oxygen ($O_2^-{}_{lat}$ > 500.0 °C). Physically adsorbed oxygen (O_{2ad}) typically desorbs below 50.0 °C. The findings indicate a desorption process of $O_{2ad} \rightarrow O_2^-{}_{ad} \rightarrow O^-_{ad} \rightarrow O_2^-{}_{lat}$ for the oxygen species adsorbed on the catalyst. Surface chemisorbed oxygen species, $O_2^-{}_{ad}$ and O^-_{ad}, demonstrate activity in oxidation reactions [57]. Table S7 presents the desorption peak area of oxygen adsorbed on various surfaces, with the desorption peak areas of Pt/AS-4-I/D, Pt/AS-3-I, and Pt/AS-2-D following NTP treatment exhibiting significantly greater values. Specifically, the desorption peak area of the INTP-DNTP synergistic regeneration catalyst increased by 14.5 and 2.5 times compared to Pt/AS-1 and the fresh sample, respectively. The order of desorption peak areas for chemisorbed oxygen species $O_2^-{}_{ad}$ was as follows: Pt/AS-4-I/D (749.57) > Pt/AS-3-I (560.28) > Pt/AS-2-D (288.79) > Fresh (213.44) > Pt/AS-1 (48.05). O_2-TPD analysis indicated that treatments with INTP and DNTP treatments resulted in enhanced production of $O_2^-{}_{ad}$ and O^-_{ad}, demonstrating synergistic regeneration. Furthermore, the desorption peaks of surface and chemisorbed oxygen shifted to lower temperatures following plasma regeneration, which suggests improved mobility of active oxygen species that may enhance catalytic activity for CO oxidation. The Pt/AS-1 catalyst treated with INTP-DNTP exhibited superior oxygen desorption capacity, increased active oxygen content, and enhanced mobility. These findings imply that plasma-synergistic regeneration significantly enhances the catalyst's oxygen activation capability, leading to a marked improvement in catalytic activity.

X-ray diffraction (XRD) analysis was conducted to evaluate the crystal structure of the catalyst before and after regeneration, with the objective of investigating its structural properties. Distinct peaks corresponding to the (111), (100), and (110) planes of Pt were clearly discernible at 2θ angles of 39.7°, 46.2°, and 64.7° across all samples, aligning with findings reported in the literature [57]. The full X-ray diffraction pattern of the Pt catalyst is presented in Fig. 4a, while Figs. S12a-c (Supporting information) illustrate the Pt diffraction patterns for the catalyst subjected to NTP treatment and aged catalyst samples within the 2θ range of 35°−45°. Compared to Pt/AS-1, Pt/AS-2-D, and Pt/AS-3-I regenerated *via* NTP, weaker diffraction peaks were observed at $2\theta = 39.7°$ In contrast, Pt/AS-4-I/D regenerated through INTP-DNT exhibited a stronger diffraction peak at $2\theta = 39.7°$. In addition to the observable peak of Pt, the catalyst samples of Pt/AS-1, Pt/AS-2-D, and Pt/AS-3-I displayed a PtO_2 (100) diffraction peak at $2\theta = 33.9°$, indicating Pt oxidation under elevated temperature oxidation conditions, consistent with the earlier XPS data. Following the INTP-DNTP synergistic regeneration modification, the PtO_2 (100) diffraction peak disappeared in Pt/AS-4-I/D, possibly due to plasma shock-induced electron temperature facilitating the decomposition of PtO/PtO_2 into Pt. Furthermore, the Pt/AS-4-I/D samples exhibited distinct diffraction peaks at $2\theta = 39.9°$, providing evidence for the presence of Pt particles generated during the INTP-DNTP synergistic regeneration process [58]. Gracia *et al.* previously reported that Pt catalysts have the capability to generate Pt metal during CO oxidation. It was suggested that Pt metal serves as the active phase for CO oxidation [59], a finding consistent with the observed increase in Pt^0 content in the XPS data.

The Pt particle size was determined using the Scherrer formula based on the full width at half maximum (FWHM) [60]. Table S8 illustrates a decreasing trend in particle size for Pt/AS-1, Pt/AS-2-D, Pt/AS-3-I, and Pt/AS-4-I/D, with Pt/AS-4-I/D exhibiting the smallest size value, which is consistent with the diminishing particle size pattern observed *via* transmission electron microscope (TEM) analysis. While there were discrepancies between the results obtained from TEM and the Scherrer formula, these variations could be attributed to technological sensitivity [61]. Nevertheless, both methods indicated a consistent trend in particle size distribution. Specifically, the findings suggest that plasma treatment of aged catalysts is beneficial for reducing the particle size of noble metal catalysts. Table S9 presents the characterization data for the specific surface area, pore volume, and pore diameter of the catalyst and carrier following plasma treatment. Analysis of Table S9 reveals a notable increase in both the specific surface area and pore diameter of the catalyst after NTP treatment. Specifically, the specific surface areas are ranked as follows: Fresh (135.78 m^2/g) > Pt/AS-4-I/D (133.68 m^2/g) > Pt/AS-3-I (130.82 m^2/g) > Pt/AS-2-D (95.93 m^2/g) > Pt/AS-1 (94.57 m^2/g). Figs. 4b and c show that the specific surface area of the Pt/AS-3-I catalyst sample treated with INTP exhibited a significant increase of nearly 40 % compared to the specific surface area of the aged Pt/AS-1 catalyst sample. Furthermore, the specific surface area of the Pt/AS-4-I/D catalyst sample, subjected to INTP-DNTP treatment with regeneration, experienced a slight increase (2.8553 m^2/g). The pore size and specific surface area data exhibited similar patterns. The hierarchy of pore sizes was as follows: Pt/AS-3-I (10.5120 nm) > Pt/AS-4-I/D

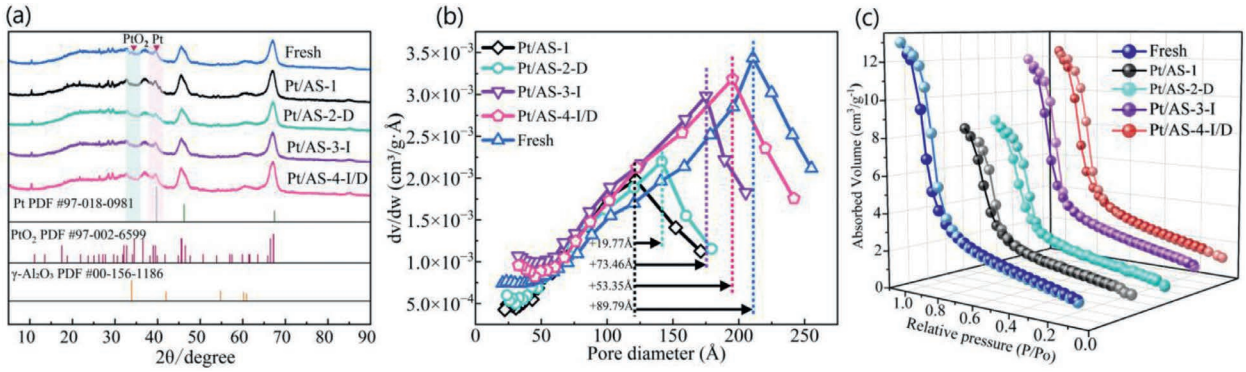


Fig. 4. (a) XRD full spectrum. (b) Pore size distribution curve. (c) N_2 Adsorption isothermal.

(9.5430 nm) > Pt/AS-2-D (9.4427 nm)>Pt/AS-1 (9.1037 nm). It was demonstrated that the presence of large mesopores was crucial for achieving optimal catalytic activity by mitigating mass transfer limitations and preventing catalyst deactivation from fouling [62]. The observed variations in specific surface area and pore diameter were primarily attributed to the active species generated by NTP using O_2 as the feed gas, facilitating the removal of particles and contaminants from the catalyst and support surfaces, as supported by XPS analysis. Furthermore, the direct discharge of DNTP was found to physically etch the catalyst surface, leading to the decomposition and shortening of catalyst and support nanorods, thereby enhancing the dispersion of aged catalysts [63,64]. The catalytic activity of a catalyst is influenced not only by the catalyst itself but also by the interactions between precious metals and supports, a phenomenon known as metal-support interaction (MSI). Scanning electron microscope (SEM) images presented in Figs. S13a and b illustrate the samples Pt/AS-1 and Pt/AS-4-I/D, revealing that the migration of loaded particles is affected by several factors, including temperature, particle size, and the surface irregularities of the support. Initially, the surface of the Pt/AS-1 support appears dense and smooth. However, after NTP synergistic treatment, the surface roughness increases, disrupting the continuous dense surface and resulting in the emergence of additional surface defects and pores [65], which aligns with the previously discussed Brunauer emmet teller (BET) results. The mobility of supported particles is not only influenced by their size but also by the morphology of the support. Micropores on the surface of the support play a crucial role in impeding particle migration. Smaller particles situated located on concave surfaces exhibit lower mobility compared to larger particles on convex surfaces [66], thereby enhancing the long-term efficiency of the catalyst.

Figs. 5a-e illustrate the size distributions of Pt nanoparticles in catalyst samples. An analysis of high-resolution transmission electron microscopy (HR-TEM) images, along with the Fig. 5b for Pt/AS-1 following thermal aging reveals an uneven size and spatial distribution of Pt nanoparticles. This phenomenon is primarily attributed to the agglomeration of the noble metal catalyst at elevated exhaust gas temperatures. The particle size distribution exhibits a bimodal pattern, with larger Pt particles ranging from 8.0 nm to 22.0 nm, yielding an average size of approximately 12.99 ± 2.792 nm. In contrast, the regenerated noble metal catalyst demonstrates Pt nanoparticles with a more uniform size and spatial distribution. The catalyst particle size distribution for Pt/AS-3-I in Fig. 5c exhibits a bimodal pattern, whereas the particle size distribution of the Pt/AS-2-D and Pt/AS-4-I/D samples in Figs. 5d and e demonstrates a unimodal distribution. Following plasma regeneration of aged catalysts, a notable reduction in the particle size of the noble metal catalysts is observed. Specifically, Fig. 5f illustrates that the average particle size of Pt/AS-4-I/D in the regenerated sample is the smallest, measuring approximately 8.25 ± 2.73 nm, which approaches the particle size of the fresh catalyst at 4.58 ± 1.65 nm as depicted (Fig. 5e). For Pt nanoparticles in Pt/AS-2-D, Pt/AS-3-I, and Pt/AS-4-I/D catalysts, the particle sizes decreased by 2.85, 3.87, and 4.74 nm, respectively, compared to the Pt/AS-1 aged catalyst samples. Notably, NTP synergistic treatment, the Pt nanoparticle size distribution exhibited a broader range skewed towards smaller sizes compared to the Pt/AS-1 aged catalyst samples. These results indicate that INTP-DNTP synergistic regeneration treatment effectively enhances the both size and spatial distribution of Pt nanoparticles.

The impact of NTP regeneration on the morphology of Pt nanoparticles within the catalyst was investigated using HR-TEM (Figs. 6b-f, 6t-z). Lattice images derived from HR-TEM images (Figs. 6u and t) reveal significant lattice distortion in the Pt/AS-1 noble metal catalyst compared to the fresh sample, which may be attributed to Pt sintering induced by elevated exhaust gas temperatures [67]. The Pt/AS-2-D, Pt/AS-3-I, and Pt/AS-4-I/D samples, following NTP regeneration treatment exhibited lattice spacings of 0.231 nm, 0.223 nm, and 0.225 nm, respectively (Fig. 6z) [68]. The morphology of Pt particles dictates the distribution of Pt sites and crystal planes on various surfaces, thereby influencing catalytic performance [69]. Examination of Pt nanoparticles in the aged catalyst (Figs. 6h and n) reveals a combination of rectangular, irregular, and spherical shapes. Pt nanoparticles exhibit diverse structures following regeneration through different methods. For instance, direct regeneration through DNTP results in a truncated triangular pyramid structure (Figs. 6i and p), whereas regeneration in an INTP oxidation environment yields an ellipsoidal shape for the Pt/AS-3-I sample (Figs. 6j and q). Furthermore, regeneration *via* INTP-DNTP produces a cubic octahedral structure (Figs. 6k and s), characterized by well-defined geometry with distinct edges and facets (Figs. 6g and m). These morphologies correspond to the typical structure of fresh DOC-coated noble metal catalysts. Previous studies have demonstrated that reducing the size of metal nanoparticles can enhance catalytic activity by increasing the exposure of catalytically active corner or edge sites on the metal surface [30,70–72]. Theoretically, smaller nano octahedra are anticipated to improve catalytic efficiency by increasing the atomic utilization of Pt and maximizing the Pt ratio at edges and vertices compared to facets [73]. TEM analysis indicates that aged Pt particles undergo reverse shape transformation following synergistic regeneration treatment with INTP-DNTP (Fig. 6a). This transformation exposes additional active sites, particularly at the edges and vertices, significantly contributing to the restoration of catalytic activity in the aged catalyst [74–76].

Fig. 7 elucidates the catalytic oxidation mechanism of the regenerated INTP-DNTP catalyst in conjunction with the aforementioned study findings of this study. The treatment of the aged cat-

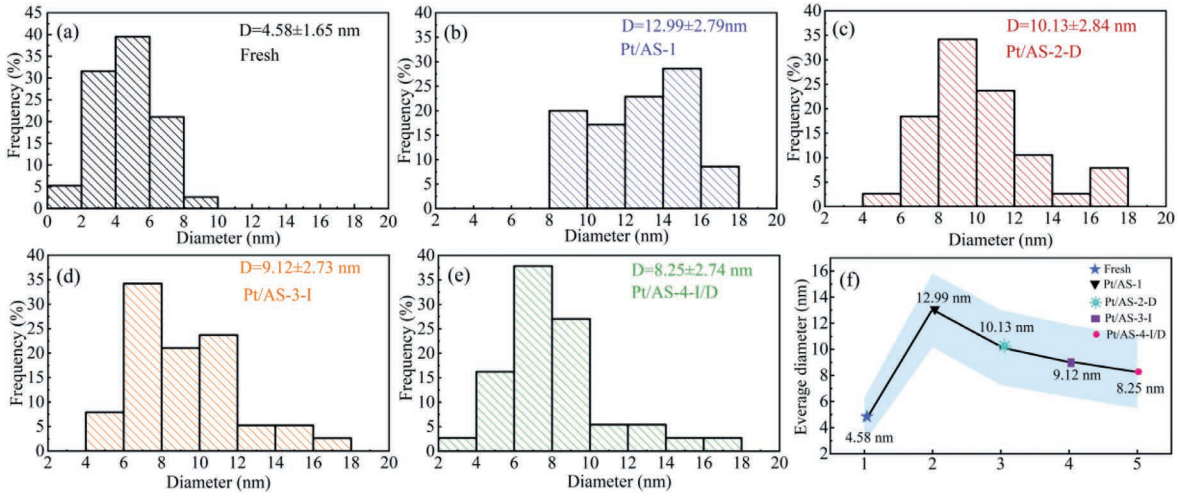


Fig. 5. Particle size catalyst particle size data obtained by TEM. (a) Fresh, (b) Pt/AS-1, (c) Pt/AS-2-D, (d) Pt/AS-3-I, (e) Pt/AS-4-I/D. (f) Catalyst particle size change trend.

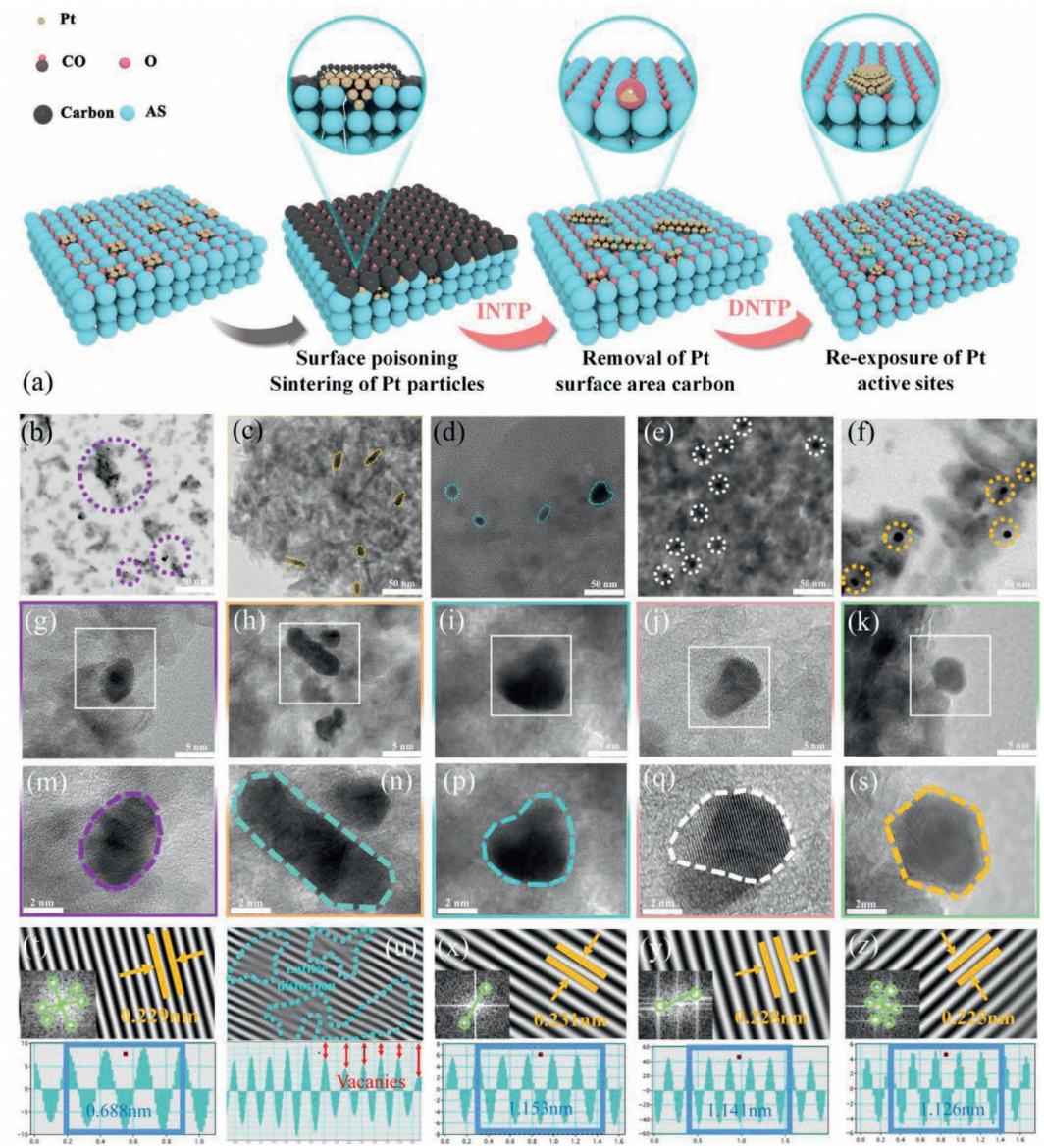


Fig. 6. (a) Diagram of NTP regeneration mechanism. Morphology of catalyst Pt microscopic 50 nm: (b) Fresh, (c) Pt/AS-1, (d) Pt/AS-2-D, (e) Pt/AS-3-I, (f) Pt/AS-4-I/D. Morphology of catalyst Pt microscopic 5 nm. (g) Fresh, (h) Pt/AS-1, (l) Pt/AS-2-D, (j) Pt/AS-3-I, (k) Pt/AS-4-I/D. Morphology of catalyst Pt microscopic 2 nm: (m) Fresh, (n) Pt/AS-1, (p) Pt/AS-2-D, (q) Pt/AS-3-I, (s) Pt/AS-4-I/D. Catalyst lattice fringe distribution and the corresponding FFT map: (t) Fresh, (u) Pt/AS-1, (x) Pt/AS-2-D, (y) Pt/AS-3-I, (z) Pt/AS-4-I/D.

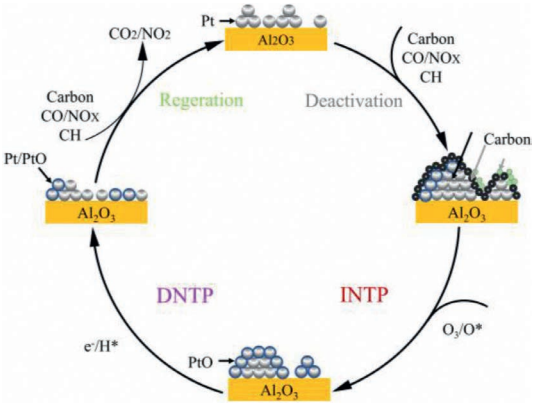


Fig. 7. Schematic diagram of the catalytic oxidation performance of the INTP-DNTP coupled synergistic regeneration catalyst.

alyst with INTP leads to in the efficient removal of PM and toxic exhaust products from the catalyst surface, facilitated by a significant amount of ozone and active oxygen. However, the exposed Pt catalyst undergoes further oxidation to platinum oxide (PtO/PtO_2), with the oxidation process intensifying as the adsorbed oxygen content increases. Following DNTP treatment, the Pt content in the Pt/AS-2-D sample increases to 23.54%, potentially attributed to the breakdown of oxides like PtO/PtO_2 by high-energy electrons generated by DNTP. Pt nanoparticles act as active sites for the activation of molecular O_2 in CO oxidation on Pt catalysts, with metallic Pt proving to be more effective than its oxidized form due to its superior electron transfer capability to O_2. Subsequent regeneration through the INTP-DNTP coupling raises the Pt content in Pt/AS-4-I/D to 33.26%. The synergy between metallic Pt and Pt oxide enhances their activity, emphasizing the concept of "metal-oxide synergy." The INTP-DNTP synergistic regeneration system employs various methods to precisely modulate the chemical state of catalyst surface elements, enabling the reversible alteration of the morphology and crystal structure of aged Pt catalysts.

This work employed NTP regeneration technology to effectively restore aged DOC catalysts with enhancing their dispersion and catalytic activity through the utilization of a plasma coupling regeneration system. Following INTP-DNTP regeneration, the characteristic temperatures $T_S/T_{50}/T_{90}$ of the aged Pt catalyst exhibited a notable decrease, resulting in a significant restoration of oxidation activity at low temperatures that closely approximates the catalytic performance of a fresh catalyst. Moreover, there was a significant increase in both the species and content of oxygen adsorption. The high valence state PtO_x was efficiently reduced to metallic Pt^0, as evidenced by the increase in the Pt/AS-4-I/D ratio from 6.84% to 33.26%. Simultaneously, the activation of surface oxygen on the DOC was enhanced through the synergistic effect of Pt^0 reduction by DNTP, which led to improvement in the catalytic oxidation capability of the DOC. The particle size of the Pt catalyst exhibited the most pronounced reduction and the particle size distribution predominantly concentrated in the low nanometer range. Furthermore, the morphology of the Pt catalyst transitioned from a strip form to small nanooctahedra. INTP-DNTP effectively facilitated the inverse transformation of catalyst morphology, significantly reducing the particle size of sintered and agglomerated Pt catalyst particles, thereby achieving realize the re-dispersion of Pt nanoparticles.

Declaration of competing interest

The authors declare that they have no known competing financial interests or personal relationships that could have appeared to influence the work reported in this paper.

CRediT authorship contribution statement

Yunxi Shi: Writing – original draft, Software, Resources, Project administration, Methodology, Investigation, Funding acquisition, Formal analysis, Data curation, Conceptualization. **Dongjie Cheng:** Writing – original draft, Visualization, Validation, Software, Methodology, Investigation, Formal analysis, Data curation. **Yi Liu:** Writing – original draft, Software, Resources, Methodology, Investigation, Formal analysis, Data curation. **Xinyi Huang:** Writing – original draft, Software, Resources, Methodology, Investigation, Formal analysis, Data curation. **Pan Wang:** Writing – original draft, Software, Resources, Methodology, Investigation. **Zhenguo Li:** Writing – original draft, Software, Resources, Methodology, Investigation. **Jizhou Jiang:** Writing – review & editing, Validation, Supervision, Software, Resources, Project administration, Methodology, Investigation, Funding acquisition, Conceptualization.

Acknowledgments

This work was sponsored by the National Natural Science Foundation of China (Nos. 52276115, 62004143), the Key Project of Scientific Research Plan of Hubei Provincial Department of Education (No. D20241501), the Major Project of Natural Science Research in Colleges and Universities of Jiangsu Province (No. 21KJA470001), the National College Students Innovation and Entrepreneurship Training Program (No. 202410299069Z), and the Innovation Project of Engineering Research Center of Phosphorus Resources Development and Utilization of Ministry of Education (No. LCX202404). We extend our gratitude to Ms. Meihong Tan (from Scientific Compass www.shiyanjia.com) for providing invaluable assistance with the TEM analysis.

Supplementary materials

Supplementary material associated with this article can be found, in the online version, at doi:10.1016/j.cclet.2025.112246.

References

[1] J. Cui, Y. Tan, J. Tan, et al., J. Environ. Chem. Eng. 12 (2024) 111930.
[2] N.E. Alexis, C. Carlsten, Int. Immunopharmacol. 23 (2014) 347–355.
[3] J. Fang, X. Xu, Y. Yang, et al., J. Therm. Anal. Calorim. 150 (2025) 7335–7347.
[4] Q. Yu, Y. Feng, X. Tang, et al., Chin. Chem. Lett. 33 (2022) 3087–3090.
[5] L. Chen, D. Weng, J. Wang, et al., Chin. J. Catal. 39 (2018) 1804–1813.
[6] H. Caliskan, K. Mori, Energy 128 (2017) 128–144.
[7] J. Fang, K. Wang, P. Chen, et al., Molecules 30 (2025) 1161.
[8] L. Gu, X. Chen, Y. Zhou, et al., Chin. J. Catal. 38 (2017) 607–615.
[9] J. Myers, Z. Chen, Chin. Chem. Lett. 26 (2015) 449–454.
[10] M.H. Wiebenga, C.H. Kim, S.J. Schmieg, et al., Catal. Today 184 (2012) 197–204.
[11] D. Duprez, M.C. DeMicheli, P. Marecot, et al., J. Catal. 124 (1990) 324–335.
[12] A. Malti, A. Kardani, A. Montazeri, et al., Powder. Technol. 386 (2021) 30–39.
[13] P. Konova, A. Naydenov, C. Venkov, et al., J. Mol. Catal. A 213 (2004) 235–240.
[14] E.T.C. Vogt, D. Fu, B.M. Weckhuysen, Angew. Chem. Int. Ed. 62 (2023) e202300319.
[15] T.N. Nguyen, Z. Chen, A.S. Zeraati, et al., J. Am. Chem. Soc. 144 (2022) 13254–13265.
[16] S. Shao, Z. Ye, J. Sun, et al., Fuel 330 (2022) 125420.
[17] Z. Chen, Y. Peng, J. Chen, et al., Environ. Sci. Technol. 54 (2020) 14465–14473.
[18] G. Petitpas, J.D. Rollier, A. Darmon, et al., Angew. Chem. Int. Ed. 32 (2007) 2848–2867.
[19] V. Vaiano, G. Iervolino, Catalysts 11 (2021) 509.
[20] Y. He, W. Sang, W. Lu, et al., Water 14 (2022) 1351.
[21] K. Li, J. Ji, Y. Gan, et al., Chin. Chem. Lett. 33 (2022) 434–437.
[22] Y. Zhu, C. Li, H. Cui, et al., J. Food Eng. 266 (2020) 109696.
[23] H. Cui, H. Li, M.A. Abdel-Samie, et al., Innovative Food Sci. Emerg. Technol. 67 (2021) 102571.
[24] J. Liu, W. Hao, Z. He, et al., Food Funct. 10 (2019) 2847–2860.
[25] H. Fan, C. Shi, X. Li, et al., Appl. Catal. B 119-120 (2012) 49–55.
[26] X. Tang, K. Li, H. Yi, et al., Phys. Chem. C 116 (2012) 10017–10028.
[27] X. Zhu, T. Wang, M.A. Serageldin, et al., Ind. Eng. Chem. Res. 62 (2023) 15434–15448.
[28] H.H. Kim, S. Tsubota, M. Daté, et al., Appl. Catal. A 329 (2007) 93–98.
[29] X. Chen, Y. Shi, Y. Cai, et al., Carbon Lett. 34 (2024) 1075–1089.
[30] L. Liu, S. Das, Z. Zhang, et al., ACS Appl. Mater. Interfaces 14 (2022) 5363–5375.
[31] P. Boutikos, J. Brezina, A.B. Arvajová, et al., Chem. Eng. J. 377 (2019) 119654.

[32] C. Hwang, C. Yeh, J. Mol. Catal. A 112 (1996) 295–302.
[33] S. Dou, L. Tao, R. Wang, et al., Adv. Mater. 30 (2018) e1705850.
[34] X. Zhang, J. Guo, P. Guan, et al., Nat. Commun. 4 (2013) 1924.
[35] J.P. Borra, N. Jidenko, J. Hou, et al., J. Aerosol Sci. 79 (2015) 109–125.
[36] J. Jiang, C. Wang, S. Zhao, et al., J. Environ. Chem. Eng. 11 (2023) 109825.
[37] X. Yu, F. Zhang, N. Wang, et al., Catal. Lett. 144 (2014) 293–300.
[38] L. Liu, Y. Liu, J. Song, et al., J. Hazard. Mater. 377 (2019) 24–33.
[39] Y. Shi, Z. Ding, Y. Luo, et al., Chem. Eng. Process. 214 (2025) 110333.
[40] B. Chen, Y. Ma, L. Ding, et al., Phys. Chem. C 117 (2013) 5800–5810.
[41] J. Ovenstone, J.I. Jung, J.S. White, et al., Solid State Chem. 181 (2008) 576–586.
[42] S.V. Moharil, B.S. Nagrare, S.P.S. Shaikh, Int. J. Hydrog. Energy 37 (2012) 5208–5215.
[43] W. Tan, S. Xie, X. Zhang, et al., ACS Appl. Mater. Interfaces 16 (2023) 454–466.
[44] T. Hyodo, T. Hashimoto, T. Ueda, et al., Sens. Actuator B 220 (2015) 1091–1104.
[45] Q. Ji, X. Yu, L. Chen, et al., Ind. Crop. Prod. 172 (2021) 114064.
[46] Y. Shi, Y. Yang, Y. He, et al., Fuel 359 (2024) 130312.
[47] C. Zhou, Y. Hu, Y. Zhou, et al., Food Chem. 445 (2024) 138699.
[48] Y. Shi, D. Hou, Y. Luo, et al., J. Environ. Chem. Eng. 12 (2024) 114772.
[49] Y. Luo, Y. Shi, K. Zhuang, et al., Processes 12 (2024) 1113.
[50] Y. Chen, J. Lin, L. Li, et al., Appl. Catal. B 282 (2021) 119588.
[51] M. Zhou, M. Li, C. Hou, et al., Chin. Chem. Lett. 29 (2018) 787–790.
[52] Q. Wu, Y. Zhong, R. Chen, et al., Ind. Crop. Prod. 222 (2024) 119676.
[53] K. Bhargavi, D. Ray, P. Chawdhury, et al., Catal. Today 423 (2023) 113998.
[54] Y. Chen, Y. Feng, L. Li, et al., ACS Catal. 10 (2020) 8815–8824.
[55] W. Liu, S. Yang, S. Liu, et al., Sep. Purif. Technol. 325 (2023) 124597.
[56] Y. Liu, D. He, Y. Chen, et al., J. Environ. Chem. Eng. 12 (2024) 113612.
[57] X. Wang, R. Li, X. Luo, et al., J. Colloid Interface Sci. 654 (2024) 454–465.
[58] J. Lee, E.J. Jang, D.G. Oh, et al., J. Catal. 385 (2020) 204–212.
[59] F.J. Gracia, L. Bollmann, E.E. Wolf, et al., J. Catal. 220 (2003) 382–391.
[60] F. Rahmani, M. Haghighi, P. Estifaee, Micropor. Mesopor. Mat. 185 (2014) 213–223.
[61] S.K. Matam, E.V. Kondratenko, M.H. Aguirre, et al., Appl. Catal. B 129 (2013) 214–224.
[62] M. Oh, M. Jin, K. Lee, et al., Chem. Eng. J. 439 (2022) 135530.
[63] C. Liu, G.P. Vissokov, B.W.L. Jang, Catal. Today 72 (2002) 173–184.
[64] J. Shi, H. Cui, J. Xu, et al., Chem. Eng. J. 389 (2020) 124459.
[65] S. Shao, T. Sun, X. Li, et al., Ind. Crop. Prod. 218 (2024) 118963.
[66] K. Narui, H. Yata, K. Furuta, et al., Appl. Catal. A 179 (1999) 165–173.
[67] X. Auvray, T. Pingel, E. Olsson, et al., Appl. Catal. B 129 (2013) 517–527.
[68] P.S. Sadalage, M.A. Dar, R.D. Bhor, et al., Food Biosci. 50 (2022) 102024.
[69] H. Mistry, F. Behafarid, E. Zhou, et al., ACS Catal. 4 (2014) 109–115.
[70] L. Zhang, L. Zhong, P. Yu, et al., Langmuir 39 (2023) 13620–13629.
[71] M. Haneda, T. Watanabe, N. Kamiuchi, et al., Appl. Catal. B 142-143 (2013) 8–14.
[72] K. Murata, E. Eleeda, J. Ohyama, et al., Phys. Chem. Chem. Phys. 21 (2019) 18128–18137.
[73] C. Li, P. Qin, G. Peng, et al., Matter 8 (2025) 102096.
[74] C. Roy, B. Sebok, S.B. Scott, Nat. Catal. 1 (2018) 820–829.
[75] C. Shen, W. Chen, C. Li, et al., J. Food Eng. 359 (2023) 111693.
[76] X. Yang, L. Ma, P. Yu, et al., J. Cereal Sci. 122 (2025) 104127.